Electronic Supplementary Material (ESI) for Energy & Environmental Science.

Supplementary Information

Influence of contouring the lithium metal/solid electrolyte interface on the critical current for dendrites

Shengming Zhang,[a] Bingkun Hu,[a] Zeyang Geng,[b] Xiangwen Gao,[a,c] Dominic Spencer-Jolly,[a,d] Dominic L.R. Melvin,[a] Ziyang Ning,[a] Guanchen Li,[b,e] Max Jenkins,[a] Longlong Wang,[a] Hui Gao,[a] Shengda D. Pu,[a] T. James Marrow,[a] Charles W. Monroe[b]* and Peter G. Bruce[a,f]*

a. Department of Materials, University of Oxford, Oxford, UK.
b. Department of Engineering Science, University of Oxford, Oxford, UK.
c. Future Battery Research Center, Global Institute of Future Technology, Shanghai Jiao Tong university, Shanghai, China
d. School of Metallurgy and Materials, University of Birmingham, Pritchatts Road, Birmingham, B15 2TT
e. James Watt School of Engineering, University of Glasgow, Glasgow, UK.
f. Department of Chemistry, University of Oxford, Oxford, UK.

*Correspondence: peter.bruce@materials.ox.ac.uk; charles.monroe@eng.ox.ac.uk

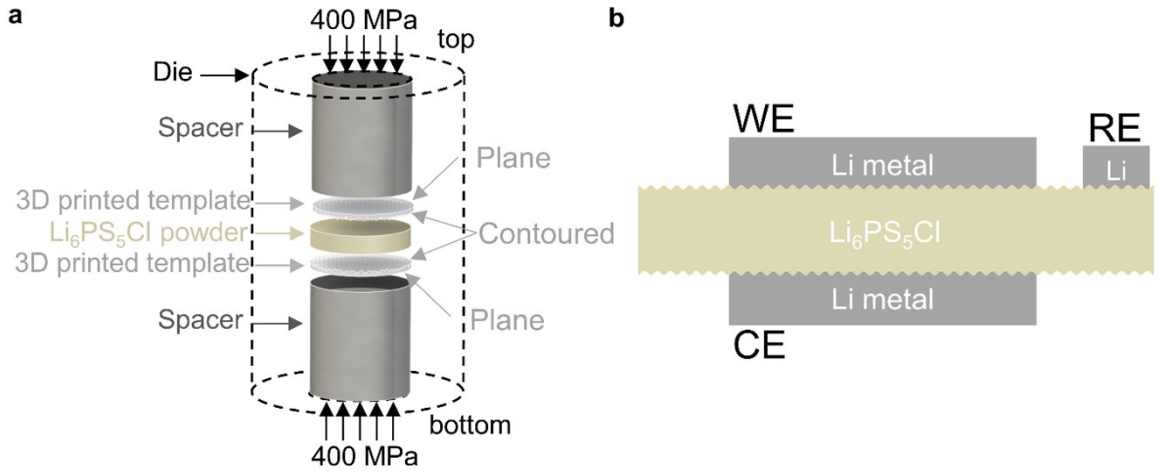

Fig. S1. (**a**) Imprinting contoured template onto a Li_6PS_5Cl disc. (**b**) Schematic of three-electrode cell with contoured Li_6PS_5Cl disc (WE: working electrode; CE: counter electrode; RE: reference electrode).

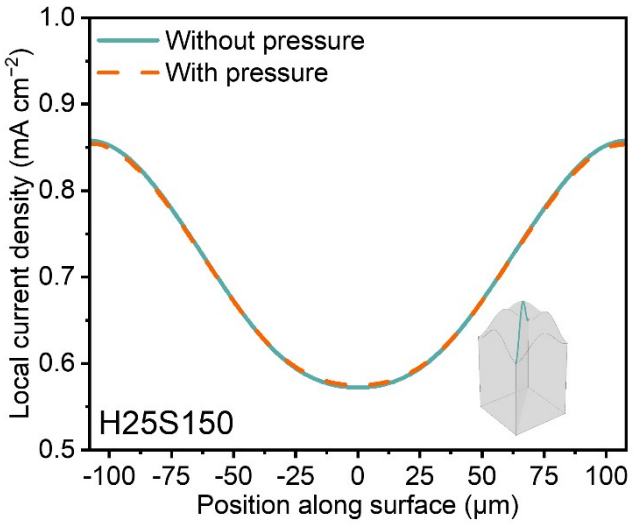

Fig. S2. The local current density is almost unaffected by whether or not the dependence of interfacial charge-transfer resistance on interfacial pressure is included in the modelling. Comparison of local current density calculated in two ways for an egg-box contoured surface with peak height (H) of 25 μm and peak separation (S) of 150 μm and 1 mA cm^{-2} geometrical current density: (orange dashed line) calculation with a kinetic rate law coupled to the local momentum balance, which includes pressure feedback in electrical boundary condition S5 through equation S16; and (teal solid line) calculation without pressure feedback, i.e., with $\rho_k(p)$ constant at $10\ \Omega \cdot cm^2$ in the rate law for charge-transfer kinetics, boundary condition S5. The inset figure illustrates the path over which local current density was taken along the diagonal direction of the egg-box surface.

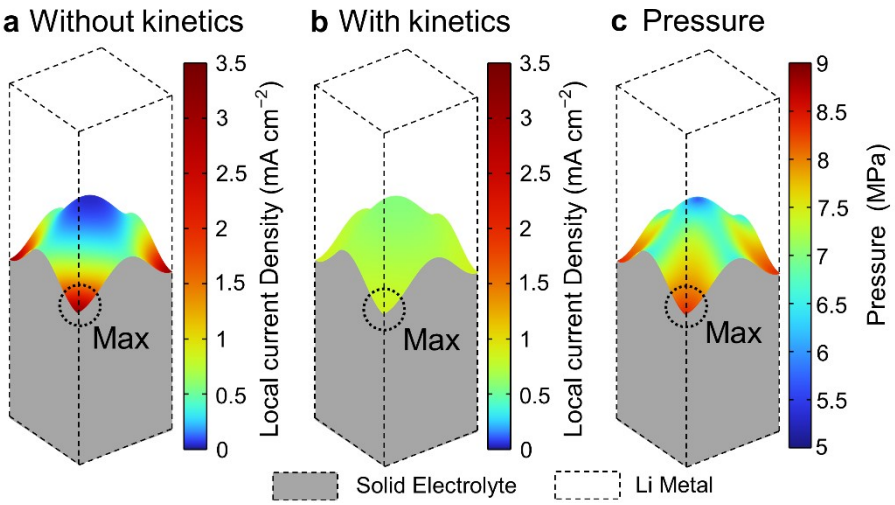

Fig. S3. Various simulation output for an egg-box contoured surface with peak height of 25 µm and peak separation of 150 µm subjected to a 1 mA cm^{-2} geometrical current density. (**a**) Local current density distribution at the Li/electrolyte interface without including reaction kinetics, i.e., assuming $\rho_k(p) = 0$ so that both sides of the interface are isopotential surfaces. (**b**) Current density distribution including kinetics (nonzero interfacial resistance of $10\,\Omega \cdot cm^2$) at the Li/electrolyte interface. (**c**) Pressure distribution calculated from current distribution including kinetics at the Li/electrolyte interface for 1 mA cm^{-2} geometrical current density.

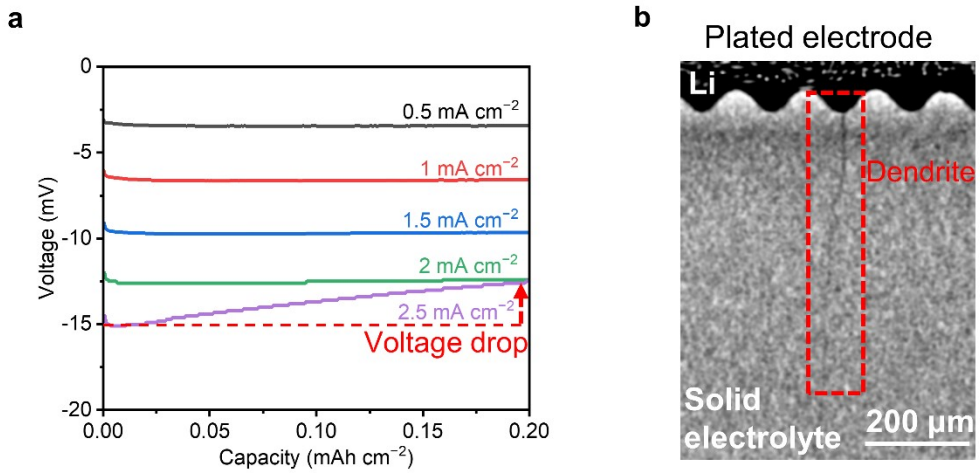

Fig. S4. (**a**) Determination of the critical current for dendrites by plating at increasing current densities with slow (0.2 mA cm^{-2}) stripping on each cycle. The critical current for dendrites is determined by a 2 mV drop, in this figure 2.5 mA cm^{-2} is the critical current for dendrite growth. The voltage response was measured using three-electrode cells, wherein any changes in polarisation can be attributed to the working electrode. A drop in the voltage during plating is widely recognised as signature of dendrite growth[1–4]. As the dendrite crack grows and lithium fills it, the contact area between the Li electrode and solid electrolyte increases, resulting in reduced polarisation. (**b**) Ex-situ X-ray computed tomography virtual cross-sectional image after the 2 mV drop showing presence of dendrite crack, which justifies that voltage drop is related to the dendrite growth.

Supplementary Text S1. Defining the 3D-printed templates

Egg-box

The egg-box surface was created by sweeping a cosine wave along the path of another identical but perpendicular cosine wave. Egg-box surfaces were generally described by the function

$$h(x,y) = H\cos(\omega x) + H\cos(\omega y) \quad \text{(S1)}$$

$$\omega = \frac{2\pi}{S} \quad \text{(S2)}$$

where H is the peak height (amplitude), ω is the wavenumber and S is the peak separation (wavelength). Peak height and peak separation are used instead of amplitude and wavelength. For instance, H25S150 is the abbreviation used for a contoured egg-box surface with peak height of 25 µm and peak separation of 150 µm. The specific dimensions for one period of a cosine wave are shown in Fig. S5a below.

The 3D-printed templates were fabricated with one contoured side, and the opposing side flat. The diameter of 3D-printed templates was 5 mm with both x and y ranging from -2.5 mm to 2.5 mm. The total thickness of the 3D-printed templates varied because of the different peak heights. An additional 300 µm thick and 5 mm diameter solid cylinder was added as a support in all cases.

All the print job files (STL format) of the templates were drawn in AutoCad (AUTODESK) and Netfabb (AUTODESK). DeSribe software (Nanoscribe) was used to convert the STL files into the GWL files, which were loaded into NanoWrite (Nanoscribe) for printing. In this conversion process, a 1 µm slicing distance for a layer-by-layer approach with block size of 300 µm $\times$ 300 µm was selected to generate the printing trajectories.

Square pyramids

The square pyramid surface was created by the same methodology for generating the egg-box surface. The specific dimensions for one period of a triangle wave are shown in Fig. S5b.

Frustum of square pyramids

The same methodology was used to create the frustum of square pyramids surface. The specific dimensions for the trapezoidal wave are shown in Fig. S5c.

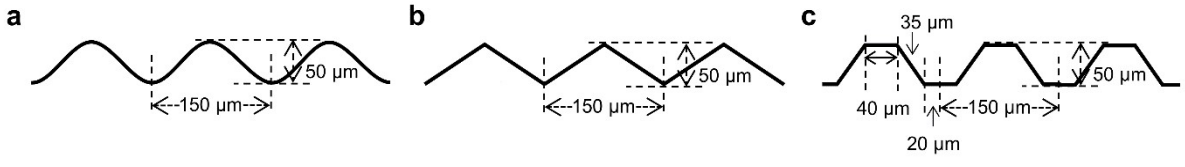

Fig. S5. (**a-c**) 2D waves for (**a**) Egg-box surfaces (cosine waves) (**b**) Square pyramidal surfaces (triangle waves) (**c**) Frustums of square pyramids surfaces (trapezoidal waves).

Supplementary Text S2. Modelling of Contoured surfaces

Simulations were taken to be periodic in the x and y directions, and interfaces were modelled using the topographies described in Fig. S5. Edge effects were neglected on the basis that the total electrode size is larger than the wavelength $2\pi/\omega$ in both the x and y directions. As illustrated in Fig. S6, the simulation ranged from $0 \leq x,y \leq S$, with the interface extending semi-infinitely away from the interface in both directions along the *z* axis (In most cases, 10H was deemed to be sufficiently far from the interface).

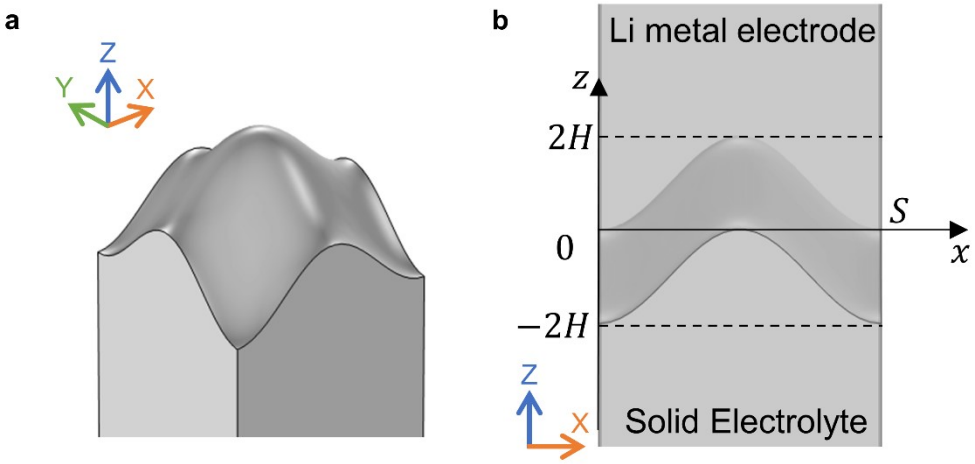

Fig. S6. (**a-b**) Li/electrolyte interface showing one period of egg-box surface with peak height (H) and peak separation (S) (**a**) 3D view and (**b**) 2D z-x plane cross-sectional view.

Model description

The 3D model comprises a steady-state electrical simulation to determine the current distribution at the interface and a mechanical simulation to determine the pressure at the interface. These two models are generally coupled through an electro-kinetic boundary condition that includes the effect of surface normal stress (i.e., interfacial pressure) on the electrochemical reaction kinetics. Model calculations were performed using COMSOL Multiphysics 6.1 software.

- **Key model assumptions**

1. The electrical and mechanical responses are in quasi-steady states.
2. The ionic conductivity of the electrolyte and electronic conductivity of the solid are constant.
3. The interface is conformal and electrical contact is uniform.
4. The lithium-plating-driven plastic flow velocity normal to the interface is directly proportional to the normal component of local current density at the surface, through the molar volume V_{Li} of lithium metal. This implies that no current goes to SEI growth, interfacial space charging, or side reactions.
5. Plastic creep of Li metal is a power-law viscous flow. No elastic response of Li metal is considered, i.e., the yield stress is assumed to be very low.
6. Lithium metal is incompressible in the pressure range of interest.
7. The solid electrolyte's elastic modulus is sufficiently high that it remains undeformed at all times.
8. Interfacial kinetics is linear with respect to overpotential and the interfacial resistance is pressure-independent (see below for justification).

9. The critical current density along a contoured surface varies with local pressure in the same way that the critical current density at a flat surface varies with global pressure.

- **Current distribution**

To model the steady-state current distribution, the lithium metal was taken to be an isopotential surface at voltage V_{ref}, on the basis that its electronic conductivity is very large compared to the ionic conductivity of the solid electrolyte. Thus, only the distributions of current density $\vec{i}(x,y\,z)$ and voltage $V(x,y,z)$ in the solid electrolyte were considered within the simulation domain $0 \le x,y \le S$ and $-\infty \le z \le h(x,y)$. The steady-state problem was modelled by combining Kirchhoff's law of the node (charge continuity) with Ohm's law (in terms of the ionic conductivity of Li_6PS_5Cl, κ) [5–7].

$$\nabla \cdot \vec{i} = 0 \tag{S3}$$

$$\vec{i} = -\kappa \nabla V. \tag{S4}$$

Kinetics of Li deposition at the Li/electrolyte interface was modelled with a Butler–Volmer equation. Fig. S7 shows that for an interfacial resistance ρ_k of the order of 10 Ω cm^2,[2,8,9] the Butler–Volmer expression is approximated well by linear kinetics if the interfacial current density is within the ±3 mA cm^{-2} range. Thus, a linear kinetic rate law was used:

$$\left(\vec{i} \cdot \vec{n}\right)\big|_{h(x,y)} = i = i_0(p)\left(e^{\frac{a_a F\left(V(x,y,h) - V_{ref}\right)}{RT}} - e^{\frac{a_c F\left(V(x,y,h) - V_{ref}\right)}{RT}}\right) \approx \frac{1}{\rho_k(p)}\left[V(x,y,h) - V_{ref}\right], \tag{S5}$$

where the surface normal vector $\vec{n}(x,y)$ points into the lithium, i is the local current density, i_0 is the exchange current density, a_a is the cathodic transfer coefficient and a_c is the anodic transfer coefficient. The linear rate law in equation S5 emphasizes that exchange current density – and consequently interfacial resistance ρ_k – generally depends on pressure, $\rho_k(p)$, as detailed in the 'Pressure effect on kinetics' section below. This dependence was accounted for to generate the data in Fig. S2, which shows that the influence of interfacial pressure on interfacial current density in this circumstance is negligibly small (a correction of ~1% or less). Unless stated otherwise, interfacial resistance was therefore assumed to be constant when generating output based on equation S5.

As z tends to –∞, the current density in the electrolyte was taken to be evenly distributed in the x and y directions, such that

$$\left(\vec{i} \cdot \vec{e}_z\right)|_{z=-\infty} = i_z = I \quad and \quad i_x|_{z=-\infty} = i_y|_{z=-\infty} = 0, \tag{S6}$$

where I is the geometrical current density. Voltage in the electrolyte was taken to satisfy periodic boundary conditions of the form

$$V(0,y,z) = V(S,y,z) \quad and \quad \left.\frac{\partial V}{\partial x}\right|_{x=0} = \left.\frac{\partial V}{\partial x}\right|_{x=S} \tag{S7}$$

$$V(x,0,z) = V(x,S,z) \quad and \quad \left.\frac{\partial V}{\partial y}\right|_{y=0} = \left.\frac{\partial V}{\partial y}\right|_{y=S} \tag{S8}$$

on the level surfaces normal to x and y at the edges of the simulation volume.

The interfacial current-density distribution determined by solving Laplace's equation (equations S3 and S4) in the limit as $\rho_k \to 0$, i.e., with $V(x,y,h(x,y)) = V_{ref}$, is shown in Fig. S3a, and the current distribution including Li deposition kinetics is shown in Fig. S3b for 1 mA cm^{-2} geometrical current density. The field enhancement effect makes the local current density highest at the points that protrude deepest into the solid electrolyte toward the counter electrode (points $x = 0$ and S, $y = 0$

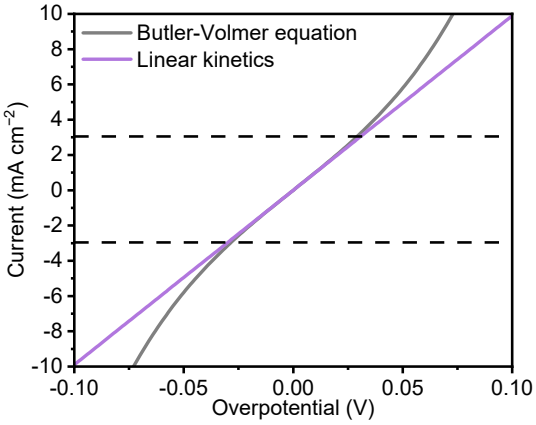

and S at $h(x,y)$ in Fig. S6); the extremity of the enhancement is lowered by interfacial resistance.

Fig.S7. Comparing the currents calculated from Butler-Volmer equation and its linearized form

- **Interfacial pressure**

The local pressure at the interface is determined both by the stack pressure externally applied to the cell (7 MPa in this work) and the dynamical pressure associated with the lithium flow away from the interface induced by the Li deposition there. The solid electrolyte was assumed to be undeformed because of its relatively high elastic modulus[10,11] compared to Li metal[12]. Thus, only the distributions of pressure $p(x,y,z)$ in the lithium metal were considered – the simulation domain is $0 \le x,y \le S$ and $h(x,y) \le z \le \infty$. The lithium plating plastic flow velocity $v_{plating}$ can be calculated directly from the local current density based on the molar volume $\bar{V}_{Li}$ of lithium metal.

$$\left(\vec{v} \cdot \vec{n}\right)\big|_{h(x,y)} = v_{plating} = \frac{i\,\bar{V}_{Li}}{F}, \tag{S9}$$

where F is Faraday's constant. The lithium was assumed incompressible, so that the flow velocity $\vec{v}$ within the metal is divergence-free. The steady-state mechanical problem was modelled by combining this incompressibility condition with the Cauchy momentum equation,

$$\rho_{Li}(\vec{v} \cdot \nabla)\vec{v} = \nabla \cdot [p\vec{I} + \vec{K}] \tag{S10}$$

$$\rho_{Li}\nabla \cdot \vec{v} = 0, \tag{S11}$$

where $\vec{I}$ is the identity matrix. The viscous stress tensor $\vec{K}$ was determined by lithium's apparent viscosity $\mu(\dot{\gamma})$–taken to be a function of its shear rate $\dot{\gamma}$–through

$$\vec{K} = \mu(\dot{\gamma})\,(\nabla\vec{v} + (\nabla\vec{v})^T). \tag{S12}$$

The relationship between the viscosity $\mu(\dot{\gamma})$ and the applied shear rate $\dot{\gamma}$ was described by a power-law creep model

$$\mu(\gamma) = m\left(\frac{\max\left(\gamma, \gamma_{low,lim}\right)}{\gamma_{ref}}\right)^{n-1}, \quad \text{(S13)}$$

where m and n are the consistency coefficient and flow behaviour index, respectively. Values of $m = 0.5 \times 10^{12}\ Pa \cdot s$ and $n = 0.11$ were used in this work, commensurate with the range of values reported in the literature ($0.47 \times 10^{12} Pa \cdot s < m < 0.68 \times 10^{12}\ Pa \cdot s$, $0.101 < n < 0.159$)[12–15]. A reference shear rate γ_{ref} of 2.828×10^{-7} s^{-1} and a lower cut-off shear rate limit of 10^{-8} s^{-1} was used[10,12].

- **Pressure effect on kinetics**

Electrochemical kinetics and interfacial kinetics interact through a pressure dependence of the electrochemical potential of electrons in the lithium, μ_{e^-}. Assuming that the partial molar volume of lithium ions in the electrolyte is small, Monroe and Newman's analysis[16] shows that the change in electronic electrochemical potential induced by a pressure at the interface is

$$\Delta\mu_{e^-} = \frac{\bar{V}_{Li}}{z_+}\Delta p, \quad \text{(S14)}$$

where z_+ is the valency of lithium ions and Δp is the pressure in the deformed lithium metal relative to an undeformed reference state. This change in electron energetics rationalises a change in the exchange current density $i_0(p)$ and thus the interfacial resistance $\rho_k(p)$, quantified as

$$i_0(p) = i_0 \mathrm{e}^{\frac{(\alpha_m - \alpha_c)z_+ \Delta\mu_{e^-}}{RT}} \quad \text{(S15)}$$

$$\rho_k(p) = \rho_k^0 / \mathrm{e}^{\frac{(\alpha_m - \alpha_c)\bar{V}_{Li}\Delta p}{RT}}. \quad \text{(S16)}$$

The mechanical transfer coefficient α_m and the cathodic transfer coefficient α_c were taken to be 1 and 0.5, respectively[16,17]. Local interfacial current densities with and without pressure coupling from the fluid flow model are shown in Fig. S2. The difference is less than 1%, and therefore the pressure effect on interfacial kinetics was neglected for this work.

- **Critical current dependency on pressure**

A linear relationship between the logarithm of the current density required for a dendrite to propagate through a solid electrolyte (i_g) and the stack pressure was recently reported[10]. The dendrite grows when the J-integral at the crack tip exceeds the fracture toughness of the solid electrolyte. For flat

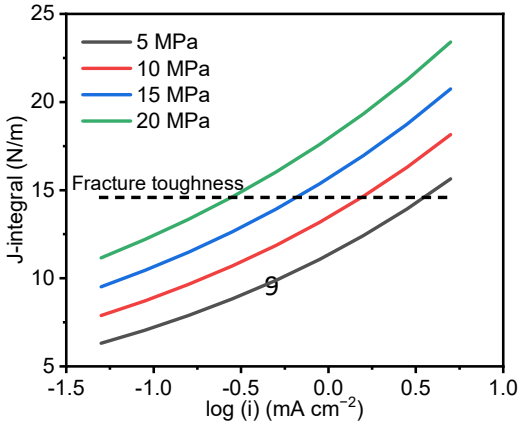

interfaces, the current density at which this occurs, i_g, is a function of stack pressure. Fig. S8 shows how the J-integral varies with pressure and current for input parameters typical of a partially-filled crack (Table S2; symbol definitions listed in Table S3).

Fig. S8. Variation of the J-integral with current density at a partially-Li-filled crack tip under different pressures.

At a given geometrical current density, the maximum local current density including kinetics and maximum pressure are calculated. The maximum local pressure is used to calculate i_g from the dendrite growth model. If the maximum local current density is lower than i_g, dendrites do not propagate. The geometrical current density is increased until the maximum local current density is equal to i_g. This geometrical current density – at which the maximum local current density and pressure become just enough to propagate a dendrite – is the calculated geometrical current density for dendrite growth.

As the H/S ratio increases, maximum local current density decreases, meaning that with the same limit for i_g from the dendrite growth model, it is possible to apply a higher geometrical current density. However, the maximum local pressure rises as H/S ratio becomes larger. This increased pressure reduces i_g, and thus the geometrical current density for dendrite growth. The impact from the increased maximum local pressure gradually outweighs the benefit of decreasing maximum local current density, leading to an increasing and then decreasing trend for calculated geometrical current densities for dendrite growth.

Table S1. i) ii) Ratio of surface area at the interface over geometrical area (cross-sectional area of the cell), i.e. surface roughness, for different combinations of peak heights (H) and peak separations (S).

i)

S (μm) \ H (μm)	5	25	50	75
150	1.02	1.44	2.26	3.19

ii)

H (μm) \ S (μm)	225	150	75	50
25	1.22	1.44	2.26	3.19

Table S2. Material properties

Parameters	Value
a	$2\ \mu m$
E	$28\ GPa$
F	$96485\ C/mol$
l_c	$287\ \mu m$
l_d	$l_c/2$
M_{Li}	$6.94\ g/mol$
m	$0.5 \times 10^{12}\ Pa \cdot s$
n	0.11
P_{stack}	$7\ MPa$
R	$8.314\ J/mol \cdot K$
T	$293.15\ K$
$\overline{V}_{Li}$	$1.3 \times 10^{-5}\ m^3/mol$
υ	0.37
α_m	1
α_a	0.5
α_c	0.5
i_0	$2.5\ mA/cm^2$
ρ_k	$10\ \Omega \cdot cm^2$
ρ_{Li}	$534\ kg/m^3$
κ	$3\ mS/cm$
$\gamma_{low,lim}$	$1 \times 10^{-8}\ 1/s$
γ_{ref}	$2.828 \times 10^{-7}\ 1/s$

Table S3. List of symbols

a	Crack width, μm
E	Young's modulus, Pa
F	Faraday constant, C/mol
l_c	Crack length, μm
l_d	Lithium dendrite length, μm
H	Peak height, μm
I	Geometrical current density, mA/cm^2
$\vec{I}$	Identity matrix, unitless
$\vec{i}$	Current density vector, mA/cm^2
i	Local current density, mA/cm^2
i_g	Current density required for a dendrite to grow through a solid electrolyte, mA/cm^2

i_0	Exchange current density, mA/cm^2
J	J-integral, N/m
$\vec{K}$	Viscous stress tensor, N/m^2
M_{Li}	Molar mass of lithium metal, g/mol
m	Fluid consistency coefficient, $Pa \cdot s$
n	Flow behaviour index, unitless
$\vec{n}$	Normal vector, unitless
p	Pressure, Pa
P_{stack}	Stack pressure, Pa
R	Gas constant, $J/mol \cdot K$
S	Peak separation, μm
T	Temperature, K
$\vec{v}$	Velocity vector, m$/s$
V	Voltage, V
$\overline{V}_{Li}$	Partial volume of Li in lithium metal, m^3/mol
υ	Poisson's ratio, unitless
z_+	Valency of lithium ion
α_m	Mechanical transfer coefficient, unitless
α_a	Anodic transfer coefficient, unitless
α_c	Cathodic transfer coefficient, unitless
ρ_k	Interfacial resistance, $\Omega \cdot cm^2$
ρ_{Li}	Density of lithium metal, kg/m^3
κ	Electrolyte conductivity, mS/cm
Γ	Integration path for J-integral
$\gamma_{low,lim}$	Lower shear rate limit, $1/s$
γ_{ref}	Reference shear rate, $1/s$
γ	Shear rate, $1/s$
μ_{e^-}	Electrochemical potential of electrons, J/mol

Reference

1 H. Wan, Z. Wang, S. Liu, B. Zhang, X. He, W. Zhang and C. Wang, *Nat. Energy 2023*, 2023, 1–9.

2 J. Kasemchainan, S. Zekoll, D. S. Jolly, Z. Y. Ning, G. O. Hartley, J. Marrow and P. G. Bruce, *Nat. Mater.*, 2019, **18**, 1105-+.

3 E. Kazyak, R. Garcia-Mendez, W. S. LePage, A. Sharafi, A. L. Davis, A. J. Sanchez, K. H. Chen, C. Haslam, J. Sakamoto and N. P. Dasgupta, *Matter*, 2020, **2**, 1025–1048.

4 D. K. Singh, A. Henss, B. Mogwitz, A. Gautam, J. Horn, T. Krauskopf, S. Burkhardt, J. Sann, F. H. Richter and J. Janek, *Cell Reports Phys. Sci.*, 2022, **0**, 101043.

5 P. R. Rayavarapu, N. Sharma, V. K. Peterson and S. Adams, *J. Solid State Electrochem.*, 2012, **16**, 1807–1813.

6 J. Auvergniot, A. Cassel, D. Foix, V. Viallet, V. Seznec and R. Dedryvere, *Solid State Ionics*, 2017, **300**, 78–85.

7 R. P. Rao and S. Adams, *Phys. Status Solidi a-Applications Mater. Sci.*, 2011, **208**, 1804–1807.

8 S. Wenzel, S. J. Sedlmaier, C. Dietrich, W. G. Zeier and J. Janek, *Solid State Ionics*, 2018, **318**, 102–112.

9 J. Su, M. Pasta, Z. Ning, X. Gao, P. G. Bruce and C. R. M. Grovenor, *Energy Environ. Sci.*, 2022, **15**, 3805–3814.

10 Z. Ning, G. Li, D. L. R. Melvin, Y. Chen, J. Bu, D. Spencer-Jolly, J. Liu, B. Hu, X. Gao, J. Perera, C. Gong, S. D. Pu, S. Zhang, B. Liu, G. O. Hartley, A. J. Bodey, R. I. Todd, P. S. Grant, D. E. J. Armstrong, T. J. Marrow, C. W. Monroe and P. G. Bruce, *Nat. 2023 6187964*, 2023, **618**, 287–293.

11 M. Papakyriakou, M. Lu, Y. Liu, Z. Liu, H. Chen, M. T. McDowell and S. Xia, *J. Power Sources*, 2021, **516**, 230672.

12 A. Masias, N. Felten, R. Garcia-Mendez, J. Wolfenstine and J. Sakamoto, *J. Mater. Sci.*, 2019, **54**, 2585–2600.

13 J. E. Darnbrough, J. Aspinall, M. Pasta and D. E. J. Armstrong, *SSRN Electron. J.*, , DOI:10.2139/SSRN.4257754.

14 W. S. LePage, Y. Chen, E. Kazyak, K.-H. Chen, A. J. Sanchez, A. Poli, E. M. Arruda, M. D. Thouless and N. P. Dasgupta, *J. Electrochem. Soc.*, 2019, **166**, A89.

15 C. D. Fincher, D. Ojeda, Y. Zhang, G. M. Pharr and M. Pharr, *Acta Mater.*, 2020, **186**, 215–222.

16 C. Monroe and J. Newman, *J. Electrochem. Soc.*, 2004, **151**, A880.

17 T. F. Fuller, M. Doyle and J. Newman, *J. Electrochem. Soc.*, 1994, **141**, 1–10.